Ocean Sci. Discuss., 9, 3485–3520, 2012
www.ocean-sci-discuss.net/9/3485/2012/
doi:10.5194/osd-9-3485-2012

Ocean Science Discussions

Mapping flow distortion on oceanographic platforms using computational fluid dynamics

N. O'Sullivan and B. Ward

School of Physics and Ryan Institute, National University of Ireland, Galway, Ireland

Received: 18 October 2012 – Accepted: 23 October 2012 – Published: 9 November 2012

Correspondence to: B. Ward (bward@nuigalway.ie)

Published by Copernicus Publications on behalf of the European Geosciences Union.

Abstract

Ocean-Atmosphere Fluxes Eddy correlation (EC) is the most direct method to measure fluxes of trace gases over the Earth's surface. In its simplest form, an EC setup consists of a gas sensor and a sonic anemometer. EC is commonly used on land, but its adaptation at sea has proven difficult because of the marine environment, the motion of the research platform (ship or buoy), and flow distortion. Flow distortion occurs when streamlines circumvent the research platform, which may lead to significant errors in the calculation of the gas transfer velocity. This paper uses computational fluid dynamics (CFD) to simulate the errors in wind speed measurements caused by flow distortion on the R/V *Celtic Explorer*. Numerical measurements were obtained from the finite volume CFD code OpenFOAM, which was used to simulate the velocity fields. This was done over a range of orientations in the test domain from -60° to $+60^{\circ}$, in increments of 10°. The simulation was also set up for a range of velocities, ranging from $5\,m\,s^{-1}$ to $25\,m\,s^{-1}$ in increments of $0.5\,m\,s^{-1}$ The numerical analysis showed close agreement to experimental measurements to within a 12 % mean difference prediction of flow distortion effects. Other aspects resulting from flow distortion that were investigated using the CFD tools included development of a correction method for flow distortion effects for in situ wind speed measurements; analysis of ideal positioning of anemometers; vertical tilt orientation of the vessel to inflow; meteorological mast design; and mast instrumentation setups.

1 Introduction

The emission of atmospheric greenhouse gas (GHG) continues to grow and the concentration of CO_2 (natural + anthropogenic) currently exceeds any level in the past 850 000 yr. Natural land and ocean sinks have removed 57 % of all CO_2 emitted from human activities during the period 1958–2008 (GCP, 2010). For the year 2008, about 25 % of all anthropogenic GHG were absorbed by oceans. The global ocean, which

OSD
9, 3485–3520, 2012

covers more than 70 % of the Earth's surface, is therefore a major sink of CO_2. However, the uptake may differ greatly from one ocean or sea to another. Accurate estimations of trace gases fluxes are needed to fully understand the climate change mechanisms. Air-sea fluxes can be estimated from measurements of atmospheric and oceanic pCO_2, the solubility s of CO_2 in sea-water and the gas transfer velocity k using:

$$F_{CO_2} = k_g \cdot s \cdot \Delta pCO_2 \quad (1)$$

The Eddy Covariance (EC) technique is the most direct method to measure fluxes of trace gases (Kondo and Tsukamoto, 2007). The EC method is used to calculate vertical turbulent fluxes within atmospheric boundary layers. This can be defined as the covariance of the vertical wind velocity and the concentration of the gas of interest over a specific time interval, typically between 10 min and 1 h (Miller et al., 2010). The air-sea CO_2 flux using the mixing ratio of CO_2 is defined as:

$$F_{CO_2} = \overline{\rho_a} \left(\overline{x_c' w'} \right)_t \quad (2)$$

where x_c is the molecular mixing ratio of CO_2 and air, $\overline{\rho_a}$ is the mean molar density of dry air during the time interval t. Equations (1) and (2) can be used to calculate the gas transfer velocity k_g. The first estimates of the gas transfer velocity through the EC method were an order of magnitude higher than those derived from the well established tracer methods (Broecker et al., 1986). Edson et al. (1998) published the first estimates that agreed with the more established tracer methods. These measurements were conducted using a closed path gas analyser to measure the CO_2 concentration to which the Webb et al. (1980) density fluctuation correction was applied. The wind speed measurements were also corrected for the ships motion using the Edson et al. (1998) motion correction algorithm.

Determining air-sea fluxes using the EC method consists of an open- or closed-path gas analyser and a sonic anemometer. The error in the EC method that will be

OSD
9, 3485–3520, 2012

addressed in this paper is flow distortion. Flow distortion occurs when streamlines circumvent the research platform (see Fig. 1), which may lead to an overestimation of the flux by approximately 15 % (Edson et al., 1998). The EC method relies on accurate measurements of wind speed to calculate the gas transfer velocity k_g. Flow distortion can be described as the difference between in-situ wind speed measurements and the un-disturbed free-stream wind speeds, which occur away from the research vessels superstructure.

One of the first attempts to define the error associated with flow distortion was a study conducted on the R/V *Aranda* by Kahma and Lepparanta (1981). Here, a mathematical correction factor was developed from the in-situ wind speed measurements and it found that the distortion effect was 10 %. Measurements were also carried out for time on an ice floe, and is more representative of wind tunnel experiments. The sea state is effectively flat since the sea surface is covered by a flat ice sheet therefore the motion of the ship is significantly damped. An anemometer was positioned on a boom 15 m ahead of the bow and these data showed considerable agreement to external measurements taken from balloon tracking results. Balloons were visually tracked with an optical instrument to give the vertical angle. The distance and horizontal angle were tracked by the ships radar. Wind speed and wind direction were then determined by the angular change over a specific time interval. These results indicated that the optimum anemometer position should be as far as possible from the platform's superstructure for undisturbed flow.

A series of complex potential flow models (i.e. steady, inviscid, incompressible and irrotational flow) was used by Oost et al. (1994) to find corrections for flow distortion. This was based on the sum of episodal and spherical shapes, which could be applied to different ships and instrumentation configurations. Each shape was solved for potential flow equations and a correction was developed from the sum of the associated errors for each shape. Oost et al. (1994) concluded that the numerical correction models were not accurate for the spatial definitions of the structure, and that wind tunnel testing of scaled physical models is more suitable. Surry et al. (1989) and Thiebaux (1990) used

OSD
9, 3485–3520, 2012

wind tunnel testing of scaled physical models to estimate the air flow over the Canadian research ships R/V *Hudson* and R/V *Dawson*. The results showed an increase of 7 % in air-flow over anemometer sites located above the ship's bridge. Brut et al. (2002) used scaled physical models in a water flume and showed that the mast on which the anemometer is mounted can have a dramatic effect on the airflow measurements.

Physical models have limitations but can be used to describe the mean flow distortion. However, in order to model the distortion effects on turbulent fluxes, the turbulent length scale must also be scaled (Popinet et al., 2004). The turbulent length scale describes the size of the large energy-containing eddies in a turbulent flow. To define these structures a sub-scale Large Eddy Simulation (LES) must be employed. The most appropriate available method to achieve this is to use CFD, which requires a numerical mesh that depends on the research platform's shape. The numerical mesh is used to solve partial differential equations between adjacent cells. CFD modeling for the quantification of flow distortion for EC measurements was first conducted by Yelland et al. (1998) for the RSS Discovery and the RSS Charles Darwin. They used the software package Vectis to predict the airflow distortion at various anemometer sites. Vectis is a commercial software package which utilises a three-dimensional Reynolds Averaged Navier-Stokes (RANS) solver. The simulations predicted that wind speed measurements are biased by approximately 10 % at certain anemometer sites. These simulated predictions were used to correct inertial dissipation measurements of the drag coefficient for the four anemometers. This led to the difference in the average drag coefficients being reduced from a maximum of 20 % for the uncorrected data to 5 % or better for the corrected data (Yelland et al., 1998). Yelland et al. (2002) showed that the numerically modelled flow distortion error agreed with the in-situ experimental wind speed measurements to within 2 % on various research ships and anemometer locations. These simulations also predicted the vertical displacement of the velocity, in order to correct the inertial dissipation method for measuring fluxes. The simulation verification was provided by comparing inertial dissipation measurements of the wind stress, obtained from instrument sites that experienced a wide range of vertical

OSD
9, 3485–3520, 2012

displacements of air-flow (Yelland et al., 2002). These showed a numerically modelled vertical displacement error ranging from 3.8 % to −15.2 %.

Popinet et al. (2004) used the more computationally expensive Large Eddy Simulation (LES) solver. LES allows for greater resolution in the turbulent regime of the simulation, as-well as more defined areas of recirculation on areas in the wake of the ships superstructure. The Gerris open-source CFD solver was used, which solves three-dimensional, time dependent Euler equations for an incompressible and inviscid fluid of constant density (Popinet, 2003). This paper involved both experimental and numerical data taken from the R/V Tangaroa. Popinet et al. (2004) showed that the mean flow characteristics are only weakly dependent on the ship motion, ship speed, wind speed or sea state, but strongly dependent on the relative wind direction. For well exposed anemometers, the wind speed measurements had a 5 % error and for anemometers in the wake of the ships superstructure there were normalised standard deviations of up to 40 %.

Griessbaum et al. (2010) used the updated GERRIS code (**?**) to define the effect of airflow distortion on estimates of the gas transfer velocity. The simulations were solved using the same method employed by Popinet et al. (2004) for two research vessels the R/V *Hakuho Maru* and the R/V *Mirai*. It was found errors ranged from −4 % to +14 % and showed that flow distortion may have a significant impact on wind speed dependent parameterisations. This can lead to possible biases in the gas transfer velocity k_g, ranging from 30 % to 50 % depending on which parameterisation is used. Griessbaum et al. (2010) concluded that the mean wind speed bias and the resulting bias in the gas transfer velocity k_g are unlikely to be corrected from one cruise period to another, even if the same platform and anemometer setup is used. As the bias varies with wind speed and with relative wind direction, the distribution in wind speed and wind direction would have to be the same in both experiments for the mean biases to cancel (Griessbaum et al., 2010).

CFD has become an established method for correcting the errors associated with direct flux measurements, and this paper deals with a CFD flow distortion study for the

OSD
9, 3485–3520, 2012

R/V *Celtic Explorer*. In this paper we report on the following: a Computer Aided Design (CAD) model of a sonic anemometer mounted on a mast, which represent the physical measurements on the R/V *Celtic Explorer*. The in-situ measurements are compared to the CFD solution and from this a correction is developed for the R/V *Celtic Explorer*. We use the CFD results to determine the ideal location for wind speed measurements on the vessel. Furthermore, we investigate the effect of varying pitch angles on the measurement data. Finally, we test two mast designs with three instrumentation setups for the optimum experimental design. Our conclusions are provided in the final section.

2 In situ measurements

Measurements were conducted on the R/V *Celtic Explorer*, where, during the period of this project, two masts were used (Fig. 2). The objective of the project was to develop an eddy correlation air-sea flux system for the research vessel. Micrometeorological measurements consisted of a Gill R3A sonic anemometer with Crossbow NAV440 inertial motion unit, as well as a Licor LI-7500 CO_2/H_2O analyser. There was also a suite of mean meteorological measurements consisting of a Young Anemometer (wind speed and direction), Vaisala temperature and humidity probe, a Druck atmospheric pressure sensor, an Eppley Radiometer (infrared radiation), and an Eppley Pyranometer (short-wave radiation). The micrometeorological and mean data were logged on a campbell CR3000 datalogger at sample rates of 10 Hz and 0.1 Hz, respectively. These in situ data provided an opportunity to compare the CFD-modelled data described below.

3 CFD modelling

The finite volume CFD code OpenFOAM 2.0.1 (OpenCFD, 2012) was used to simulate the velocity fields around the R/V *Celtic Explorer*. OpenFOAM is a C++ library used primarily to create executables, known as applications. The applications fall into two categories: solvers, designed to solve a specific problem in continuum mechanics; and

OSD
9, 3485–3520, 2012

utilities, designed to perform tasks that involve data manipulation. Two standard solvers were used for the simulations presented here:

- PotentialFOAM is a potential flow solver which can be used to generate starting fields for full Navier-Stokes codes and reduces the normal run up time instabilities associated with steady-state simulations (OpenFOAM, 2011).
- SimpleFOAM uses The Semi-Implicit Method for Pressure-Linked Equations (SIMPLE) algorithm, which allows coupling the Navier-Stokes equations with an iterative procedure (openfoamwiki, 2010).

The simulation properties outlined follows the prescribed method of setup conducted by Gagnon and Richard (2010) for the OpenFOAM implementation of the simpleFOAM steady state algorithm. The simulation properties were tested against the Ahmed body (a simplified, standardised car body used in CFD testing) wind tunnel data. There are an extensive number of experimental wind tunnel data sets, which are widely used in the validation of external aerodynamics simulations in CFD. Testing against these experimental data is considered an acceptable comparison, as the Ahmed body creates defined vortices in its wake region. The Ahmed body model also has an angled front section which allows a defined comparison of lift and drag coefficients. The conclusion from Gagnon and Richard (2010) showed that the chosen simulations setup using the simpleFOAM algorithm had a 10 % difference from experimental wind tunnel testing data. Using this setup thus gave us initial accuracy levels within 10 % of experimental data from the in-situ wind speed measurements on the R/V *Celtic Explorer* as validated by the Gagnon and Richard (2010) simulations. A time-varying velocity was applied from 5 to 25 $\mathrm{m\,s^{-1}}$ in steps of 0.5 $\mathrm{m\,s^{-1}}$ at the inlet boundary condition, which is a spatial specification of values at the domain inlet. The temporal discretion scheme (computational time step equations control) between points was defined to allow each velocity input to pass through the domain 10 times (OpenFOAM, 2011).

A Courant number of less than 1 was used for temporal accuracy and numerical stability (Souza, 2005). The Courant number is the speed of sound multiplied by the ratio

OSD
9, 3485–3520, 2012

of the time step length to the cell length. This ratio is the time required for a quantity or fluid particle to be convected through a small distance. This was also applied to improve the computational cost on running a range of velocity inputs, as well as to obtain a greater array of values to compare with experimental data. Since the ratio between model and domain size is less than 1 %, this creates an infinite domain size. The walls which are the left, right and top boundaries of the simulation domain, have little effect on the model, therefore these boundary conditions were set as symmetry planes. A symmetry plane is where the normal velocity is zero and the normal gradients of all other variables are also zero (Souza, 2005). The highly effected regions of the simulations and thus the most significant boundary conditions are the vessel surface and the floor surface (the lower boundary of the simulation domain). In accordance with Gagnon and Richard (2010), a classical log-law wall function was applied to the floor and vessel's surface for the turbulence characteristics of k (specific kinematic viscosity) and ω (specific dissipation rate). The $k-\omega$ SST (shear stress transport) turbulence model Menter (1993) was used for a turbulent intensity of 4 % for all boundary conditions, which specifies the turbulence level.

A Reynolds number of 10^8 referenced from Popinet et al. (2004) for airflow at the air-sea boundary layer in the ocean was used to calculate the kinematic viscosity of the fluid. This model is a two equation eddy viscosity model and is usable all the way down to the wall through the viscous sub layer. The model was used for its proven reliability in separation zones, and its ability to blend a good free-stream model to a good boundary layer model (Gagnon and Richard, 2010). The outputted calculations from the simulations contain logs for U (velocity), P (pressure) and k. The CAD models were generated using the 3-D solid modelling software Blender 2.60. Figure 3 shows the generated 3-dimensional model and a cross-section of the mesh refinement containing hexahedron (hex) and split-hexahedron (split-hex) cells around the R/V *Celtic Explorer* CAD model. The CAD model was scaled to 1:10, which in-turn defined a simulation domain size of $37.85 \times 20.2 \times 20.2$ m for flows directly over the bow. This CAD model scale and model domain size was chosen to give a 1 % blockage area (area ratio between the inlet of

OSD
9, 3485–3520, 2012

the simulation domain and the CAD model) of the inlet section of the wind tunnel by the test geometry as described by Castro and Robins (1977). This allows the flow to completely stabilise within the simulation domain. In the case of the R/V *Celtic Explorer*, the size of the domain is also dependent upon the ship's orientation to the flow. The width of the domain can therefore increase to over 40 m for flows over the ship's beam.

CAD models scaled to 1:1 of the two masts (Fig. 2) were also created and implemented with the same simulation setup (i.e. OpenFOAM numerical solvers, Boundary conditions and Turbulence model), as the R/V *Celtic Explorer* simulations. A 1 % inlet blockage area was also applied to the domain size and model scale. The Mast CAD models were contained within a simulation domain of 46.9 × 24.9 × 24.9 m. The Mast CAD models were also configured with 3 different instrumentation setups, containing different sonic anemometer and Licor gas analyser setups. Finally a simulation was implemented where the effect of the pitch angle of the ship on the wind speed determination was evaluated. The CAD model was tilted within the domain through orientations ranging from 0–6° in steps of 2°. The domain size and simulation setup remained the same for this model as previously used the R/V *Celtic Explorer* simulations. The CAD models were imported into OpenFOAM as an interchangeable 3-D file format. In the vessel simulations this was done over a range of orientations in the test domain, from −60° to +60° in increments of 10° giving 13 model orientations within the simulation domain. The simulation was setup for 41 different velocities, ranging from 5 to 25 $m\,s^{-1}$ in increments of 0.5 $m\,s^{-1}$. The vertical orientation of the model was done over a range of orientations in the test domain, from 0° to +6° in increments of 2° giving 4 model orientations within the simulation domain.

The simulation was also setup for 41 different velocities, ranging from 5 $m\,s^{-1}$ to 25 $m\,s^{-1}$ in increments of 0.5 $m\,s^{-1}$. The meteorological mast setup comparisons were performed for 0–60°. This simulation setup was also done for 41 different velocities, ranging from 5 $m\,s^{-1}$ to 25 $m\,s^{-1}$ in increments of 0.5 $m\,s^{-1}$. The meteorological mast setup comparisons were preformed for 2 different mast designs(Mast1 telegraph pole design and Mast2 Triangular lattice design) and 3 different instrumentation setups(Gill

OSD
9, 3485–3520, 2012

sonic anemometer, Gill sonic anemometer/Licor and Campbell sonic anemometer/Licor), giving 42 simulations in total. The total number of simulations run from all the variations tested was 59.

The OpenFOAM code was compiled with gcc-4.4 and openMPI and ran on 2 cluster computers: a Bull Novascale R422-E2 cluster with 64 compute nodes and an SGI Altix ICE 8200EX cluster with 320 compute nodes. For the former, each compute node has two 2.8 GHz Intel (Nehalem EP) Xeon X5560 quad-core processors and 48 GB of RAM, resulting in a total of 512 cores and 3072 GB of RAM available for jobs. For the latter, each compute node has two Intel (Westmere) Xeon E5650 hex-core processors and 24 GB of RAM, with a total of 3840 cores and 7680 GB of RAM available for jobs. There was a total run time of 14.5 days for the completed code using both computers. Each case was run on 64 parallel processors per case.

4 Results and discussion

In accordance with Popinet et al. (2004) two assumptions were made:

1. The wind speeds measured at different locations should scale linearly with some reference velocity, meaning the fluid flow is essentially independent of the Reynolds number.

2. The averaged velocity depends only on the relative wind direction.

The first assumption is justified as the Reynolds number ($\sim 10^8$ based on ship length and $10\,\mathrm{m\,s^{-1}}$ wind speed), is well within the asymptotic regime for flow around a solid obstacle (Popinet et al., 2004). The second assumption chooses to neglect the influence of the sea conditions as well as ship motion. It is extremely difficult to simulate ship movement as regards yaw, pitch and roll, which leads to large computational costs, therefore we chose to neglect. We do however investigate flow for various pitch angles (see Sect. 4.3).

OSD
9, 3485–3520, 2012

The experimental results were taken during a R/V *Celtic Explorer* cruise between 5 October 2008–23 October 2008 using the Mast1 design instrumentation setup (Fig. 2). The results are processed to give a true wind velocity value corrected for the ship with reference to the Earth's surface and true north. This is done for the 2 Young's mean anemometers and the 3-D Gill sonic anemometer on the bow-mast as well as ship's bridge anemometer. A 30-min averaged time-series of data for the chosen cruise period is shown in Fig. 4a. This gives a mean difference from the bow-mast sonic anemometer location to the ships bridge deck anemometer location of 1.28 m s^{-1}. From the bow-mast sonic anemometer to the bow-mast young's mean1 anemometer a mean difference of 0.27 m s^{-1} is recorded. In Fig. 4b distribution of velocities collected for the chosen cruise defining a lack of data at higher wind velocities greater than 15 m s^{-1}.

The scatter plot Fig. 5a shows the magnitude of wind speed difference between the bow-mast sonic and the ship's bridge deck anemometer with respect to the wind direction. It shows how the change in wind speed affects the difference in measurements between the 2 anemometers, and that increased distortion affects occur at 0° to the bow and −60° to the bow. This gives a representation of the varying wind speed differences, from which the magnitude of the flow distortion error for this given space ranges from +5 to −1.25 m s^{-1}. A high velocity gradient (Fig. 7) forms on the bow tip of the vessel at 0° inflow. As the orientation tends towards ±60°, the vertical component of the calculated velocity gradient in this area is reduced. However in another respect as the orientation tends towards the negative direction for high wind speed inputs a higher distortion error can be seen because of the recirculation caused by a crane being mounted on that side of the vessels bow deck. This occurs when high wind speeds impact the crane, the generated shock-wave produced causes recirculation and higher turbulence in the negative direction. However, this is not the case in the positive direction as is evident in the experimental scatter plot results (Fig. 5a).

Figure 5b shows the difference between the bow-mast sonic anemometer and the bow-mast Young's mean starboard anemometer. This shows the same trend seen in Fig. 5a, where the difference increases across this space as a function of wind speed.

OSD
9, 3485–3520, 2012

From this plot, the magnitude of the flow distortion error range was established to be of -0.2 to $+0.5\,\mathrm{m\,s^{-1}}$.

4.1 Vessel simulations

Cross-sectional contour plots for -60° and $+60^{\circ}$ inflow to the bow are shown in Fig. 6. These plots show the change in the velocity profile for the associated change in direction produce different wake structures preceding the bow mast. It can be seen for -60° there is a higher gradient of turbulence in the wake of the bow mast. This is also apparent in the experimental results shown in Fig. 5a. This is due primarily to the presence of a bow-deck crane on the port side causing increased distortion effects and recirculation at high wind speeds. This verifies the validity of the simulation results as spatially accurate to the physical reality of the experimental results.

In order to validate the simulations directly from the experimental measurements, a spatial differencing method was developed based on (Popinet et al., 2004). The comparison of the difference between simulated wind speeds from a referenced location to another location in the numerical domain should predict the difference in experimental measurements over this same space, thus giving an estimate of the accuracy of the simulations to predict a free-stream velocity occurring away from the vessels superstructure. This method is valid due to the fact that relative position of the anemometers does not change in time or space and the simulated wind speeds at different locations scale linearly with a reference velocity. The difference across the prescribed anemometer locations was calculated in the simulation results. The 3D surface plots were generated from individual line plots ranging from -60° to $+60^{\circ}$ inflow direction to the ship's bow, in steps of 10°, shown in Fig. 7. To fill the surface plots, a linear interpolation was performed between the 10° steps of the simulation prediction. This was performed to provide the differences from each calculated anemometer probe location over the same space in which experimental measurements were conducted. As this was calculated for spaces on the research vessels superstructure, it is effectively a fraction of the total

OSD
9, 3485–3520, 2012

flow distortion error for each referenced anemometer location. Flow distortion error is described as the difference from the anemometer's wind speed measurements to free-stream measurements which occur away from the research vessels superstructure.

Figure 7a and b, respectively show the outputted simulation prediction of the flow distortion error for 5–25 m s^{-1} input velocity, and ±60° inflow direction for the difference between bow-mast sonic anemometer and the Young starboard/port anemometers. The plots show peaks in the simulated error as the inflow direction aligns with the vertical (T-bar) section of the mast, thus causing elevated distortion since the instrument measurement location is in its wake. This indicates that the simulation results are spatially accurate for this 0.5 m space. It can also be seen in experimental difference plot Fig. 5b for this space, that the range of differences is 0 m s^{-1} to +0.5 m s^{-1} and contains the same peak in the negative direction. In Fig. 7c the predicted errors between the bow sonic anemometer and the ship's bridge deck anemometer shows elevated distortion in the negative direction as a result of the bow-decks crane. Comparing Fig. 7c to 5a, the same range of differences can be seen i.e. from −2 to +4 m s^{-1}. In Fig. 7d we see the surface plot prediction of errors for the bow-mast sonic anemometer location, with respect to the difference from free-stream velocity measured at 20.5 m from the bow. This space was chosen as the initial velocity predictions at the inlet of the domain can be turbulent. It also represents the space used in the prediction of the bow-mast sonic anemometer to ships bridge deck anemometer. The accuracy of this prediction to free-stream, is defined by the downstream accuracy of the bow-mast sonic anemometer to ships bridge deck anemometer, because down-stream accuracy is dependent on up-stream air-flow calculations.

Figure 8 shows the differences between the various anemometers for both the experimental and modelled data, which was derived from the datasets produced in Fig. 7. These plots show both the calculated difference for each defined space and the difference for the same space found in experimental measurements. The bow-mast sonic anemometer and the bow-mast Young's mean starboard anemometer shows an RMS value of 0.03 m s^{-1}, the bow mast sonic anemometer to the bow mast mean port

OSD
9, 3485–3520, 2012

anemometer shows an RMS value of 0.013 m s^{-1}. Finally the bow mast sonic anemometer to the ship's bridge deck anemometer shows an RMS difference value of 0.86 m s^{-1}. These difference plots are shown in Fig. 8a, b, and c, respectively. The calculated error in Fig. 8c was extracted from the measured ship bridge deck anemometer data to give a corrected data-set for this measurement location. The corrected data-set showed a mean difference of 0.18 m s^{-1} from the bow-mast sonic anemometer data-set, whereas the un-corrected original mean difference for this space was 1.45 m s^{-1}, thus leaving a 12.68 % error in the correction of this space. This directly describes the level of accuracy in the numerical prediction when compared to the measurements. Also Fig. 8c shows inputted wind direction to define that for highly fluctuating changes in wind direction, the averaged numerical models fall off, leading to errors in the accuracy of the correction. This defines that more discrete steps in direction should be simulated to improve the level of accuracy of the correction. Figure 7d corresponds to 8d, where the error found from the evaluated surface plot to free stream was extracted from the measured bow mast sonic anemometer. This gives a corrected plot of the data (in black) for the duration of the chosen cruise period. The plots show a correction range from 2.4 m s^{-1} to −1.0 m s^{-1}, with an RMS value of 0.43 m s^{-1}, and shows a percentage range of correction from −6.14 % to 10.67 % to free-stream undistorted flow.

4.2 Ideal anemometer locations

A vector plot of the velocity profile at 0° inflow to the bow is shown in Fig. 9. This plot was used to define the areas of highly deviated airflow, showing high distortion in the wake of any deck mounted structure. Deviations from the mean flow and recirculation areas can be seen upwind of the bridge deck. Highly deviated areas with recirculation can also be seen in the wake of the bridge deck. This describes the optimum area for positioning of anemometers, which should be as far towards the bow as possible, and faced into the mean free-stream airflow. In Fig. 10 there is a high-resolution grid (20955 points) within this defined area, where velocity calculations were recorded for

OSD
9, 3485–3520, 2012

each point. The difference to free-stream velocity for the chosen points ahead of the mast position were plotted for change in height (Fig. 11). This shows that the sonic anemometers current position is within a wake region caused by a forward shockwave from the bow, therefore the height should be increased to greater than 14 m. This correction was selected only for points ahead of the mast and therefore the distance from the bow can also be found. The most accurate recorded position was found to be placed in an acceleration zone at the bow as shown in Fig. 10. However, for varying directions and tilt angles, the position of the acceleration zone changes. The most accurate velocity position outside of this acceleration zone shows that the sonic anemometer should be placed 3.2 m ahead of the bow and higher than 14 m from the ship's deck. This position correction will lead to a reduction in the flow distortion error to 4 % of the measured wind speeds at the bow-mast sonic anemometer position.

4.3 Vertical orientation of model

Figure 12a and b show high-resolution velocity plots for a wind input of 25 m s^{-1} for a model pitch angle of 0° and 6° along its y-axis, respectively. What is most striking is the increase in the domain velocity of 1.2 m s^{-1}. Focussing on the sonic probe location (Fig. 13), the effect of changing the ship's pitch angle for 4 discrete angles is shown. Changing the pitch angle of the ship has a strong increase in the vertical velocity measurement from a sonic anemometer. The vertical orientation of the ship effectively creates a larger area of blockage with increasing pitch angle, resulting in a maximum distortion effect of 3.6 m s^{-1} at a high wind speeds of over 20 m s^{-1}.

4.4 Meteorological mast setup comparison

The meteorological mast setup simulations were carried out for two individual mast designs (see Fig. 2) with different instrumentation attached, which involves a Gill R3A sonic, a Campbell sonic, and Licor LI7500. Both mast designs and the instrumentation simulations were performed for a 0–60° bow-on wind. In Fig. 14 is shown velocity

OSD
9, 3485–3520, 2012

magnitude profiles around Mast1 and Mast2, each with a Campbell sonic anemometer and Licor LI7500 gas. The wake structure from Mast2 has a greater influence on instrumentation down-stream, whereas Mast1 has a more predictable gradient of turbulence in the wake of the design, which allows for a simpler correction. However, Mast1 design has a higher vertical turbulent gradient due to the lack of open sections which would allow wind to pass through the design.

A cross-sectional vector plot of the airflow divergence for the x direction uniform inflow velocity is shown in Fig. 15. This was scaled by the measured vertical component of the inflow velocity. Highly distorted wind magnitudes can be seen in the vertical direction of the plot. Anemometer measurement locations positioned directly above the control boxes can be highly affected due to the recirculation caused by the instrumentation. The Campbell sonic and Licor setup being positioned ahead of this vertical vector field are nearly free stream, defining that positions ahead of this field have little effect from the instrumentation boxes. The comparison in mast geometries was also conducted to allow a future comparison with the effects of the new measurement system deployed on the R/V *Celtic Explorer* when sufficient experimental data is obtained. The developed differences in the mast geometries can then be applied to the R/V *Celtic Explorer* simulations containing the Mast1 design. This was conducted due to the complex geometry of the Mast2 design, which would have been computationally expensive in comparison to the Mast1 design and also due to the limited amount of experimental data currently available.

5 Conclusions

It has been established that OpenFOAM simpleFOAM algorithm shows close agreement with experimental results and can be used as a valid correction for flow distortion over oceanographic platforms. It has shown a close prediction of flow distortion error to within 12 % of experimental results and predicts the same scale of error across

OSD
9, 3485–3520, 2012

each space tested. This correlates to Gagnon and Richard (2010) statement that the simpleFOAM algorithm had a 10 % difference from experimental testing.

The spatial differencing method that has been developed shows a defined method for correction of data for full cruise periods. This gave RMS values to experimental results of 0.42 m s^{-1} for 20.5 m prediction space and 0.013 m s^{-1} across a 0.5 m prediction space. It has been shown that matching the mean difference from experimental results to corrected wind speeds led to a prediction within 10 % for the 20.5 m space and 50 % for the 0.5 m space. Therefore, over a small space, the prediction of error using a steady state model is not appropriate and sub-scale LES model should be used to improve accuracy.

It has also been found that for a highly accurate correction model, a discrete selection of inflow directions should be simulated. Higher scatter is developed in these orientations as a direct effect of a crane being mounted on one side of the bow deck. In high wind speed situations, the crane causes recirculation and higher errors, which is apparent, in both numerical and experimental results. Previous research (e.g., Popinet et al., 2004; Yelland et al., 2002) concluded that wind direction and not wind speed is the dominant factor in flow distortion errors for micrometeorological measurements on research vessels. Our results here indicate that the magniture of the wind speed (as well as wind direction) is a quantity of significant importance.

The results of the mast simulations indicate the affects of a more complex geometry gives more distortion effects and errors in wind speed estimates. These simulations also show a consistency that is apparent in all the performed simulations. High wind speeds tend to have higher distortion effects, due primarily to the passage of air-flow over the surface at high velocities cause recirculation effects. The two simulated mast geometries showed that a more applicable design would be a telegraph pole like design with as little as possible blockage to the inflow wind stream. In the future, an optimised design will be developed for deployment and testing.

The comparison between different instrumentation setups showed the 3-D Campbell sonic anemometer to have less distortion effects than the 3-D Gill sonic anemometer.

OSD
9, 3485–3520, 2012

This is due primarily to its sampling probe window being ahead of the device, thus causing less impact on the mean airflow. With additional instrumentation positioned beside the anemometer e.g. a Licor LI7500 gas analyser, it was found the best position for sampling is in the wake of the anemometer. This will allow measurements at the anemometer location to be unaffected by the instruments blockage of airflow. An evaluation of instrumentation dry boxes has also described that anemometer measurement locations positioned directly above dry boxes can be highly affected. This is due to the recirculation caused by the instrumentation dry boxes and should be positioned more than 1.5 m from the dry boxes for unaffected airflow.

The ideal locations for the sonic anemometer contained 20955 chosen points for evaluation, with the best location established as the best fit for the performed simulations. This location should be as far as possible from the superstructure of the vessel and outside of its wake. It was found that the ideal location of the sonic anemometer for the R/V *Celtic Explorer* was 3.2 m ahead of the bow and an elevation 14 m from the bow deck, in order to reduce the distortion effects to 4 %.

The study of the effect of various ship pitch angles was performed, which was the first time such a study was carried out using CFD. The vertical displacement was carried out over a limited number of angles, but the results show that vertical orientation of the vessel is a quantity that affects the passing flow. Previously velocity measurements have been averaged or corrected to eliminate the motion of the platform. This has also been done here to match the vessel simulations to experimental measurements. From the performed simulations, it can be seen the vertical displacement of the vessel for all wind speeds changes distortion effects as the angle increases. The tilt of the vessel through higher angles of attack develops a higher error in the vertical component of the wind speed at low inflow velocities, thus causing higher lift and higher distortion.

Acknowledgements. This research is supported by the Irish Research Council for Science, Engineering and Technology via the Enterprise Partnership Scheme Postgraduate Scholarship Programme, grant number EPSPG/2011/249 and the EU FP7 project CARBOCHANGE under grant agreement No. 264879.

OSD
9, 3485–3520, 2012

References

Broecker, W. S., Ledwell, J. R., Takahashi, T., Weiss, L. M. R., Memery, L., Peng, T. H., ihne, B. J., and Jnnich, K. O. M.: Isotopic versus micrometeorologic ocean CO_2 fluxes:A serious conflict, J. Geophys. Res., 91, 517–10, 1986. 3487

Brut, A., Butet, A., Planton, S., Durand, P., and Caniaux, G.: Influence of the airflow distortion on air-sea flux measurements aboard research vessels: Results of physical simulations applied to the EQUALANT99 experiment, J. Amer. Meteor. Soc., 15, 147–150, 2002. 3489

Castro, I. P. and Robins, A. G.: the flow around a surface mounted cube in uniform and turbulent streams, J. Fluids. Mech., 79, 307–335, 1977. 3494

Edson, J. B., Hinton, A., Prada, K. E., Hare, J. E., and Fairall, C. W.: Direct covariance flux estimates from mobile platforms at sea, J. Atmos. Ocean. Tech., 15, 547–562, 1998. 3487, 3488

Gagnon, L. and Richard, J. M.: Parallel CFD of a prototype car with OpenFOAM, Tech. rep., Dept of Mech. Eng., Laval University, Québec, Canada, 2010. 3492, 3493, 3502

GCP: Global carbon project, http://www.globalcarbonproject.org/, last access: 30 August 2010. 3486

Griessbaum, F., Moat, B. I., Narita, Y., Yelland, M. J., Klemm, O., and Uematsu, M.: Uncertainties in wind speed dependent CO2 transfer velocities due to airflow distortion at anemometer sites on ships, J. Atmos. Chem. Phys., 10, 5123–5133, 2010, http://www.atmos-chem-phys.net/10/5123/2010/. 3490

Kahma, K. K. and Lepparanta, M.: On errors in wind speed observations on R/V *Aranda*, J. GeoPhysica, 17, 155–165, 1981. 3488

Kondo, F. and Tsukamoto, O.: Air-Sea CO_2 Flux by Eddy Covariance Technique in the Equatorial Indian Ocean, J. Oceanogr., 63, 449–456, 2007. 3487

Menter, F. R.: Improved Two-Equation $k - \omega$ Turbulence Models for Aerodynamic Flows. Turbulence Models for Aerodynamic Flows, NASA Technical Memorandum, NASA, 103975, 34 pp., 1992. 3493

Miller, S. D., Marandino, C., and Saltzman, E. S.: Ship-based measurements of air-sea CO_2 exchange by eddy covariance, J. Geophys. Res., 115, D02304, doi:10.1029/2009JD012193, 2010. 3487

OSD
9, 3485–3520, 2012

Oost, W. A., Fairall, C., Edson, J., Smith, S., Anderson, R., Wills, J., Katsaros, K., and DeCosmo, J.: Flow distortion calculations and their application in HEXMAX, J. Atmos. Ocean. Tech., 11, 366–386, 1994. 3488

OpenCFD: OpenFOAM flow solver, version 2.0.1, OpenCFD Ltd. (ESI Group), Bracknell, UK, 2012. 3491

OpenFOAM: OpenFOAM Users Guide 2011, version 2.0.1, http://www.openfoam.org/archive/2.0.0/docs/user/, last access: 24 September 2011. 3492

openfoamwiki: The Simple algorithm in OpenFoam, http://openfoamwiki.net/index.php/, last access: 26 August 2010. 3492

Popinet, S.: Gerris: A tree-based adaptive solver for the incompressible Euler equations in complex geometries, J. Comput. Phys., 190, 572–600, 2003. 3490

Popinet, S., Smith, M., and Stevens, C.: Experimental and numerical study of the turbulence characteristics of airflow around a research vessel, J. Atmos. Ocean. Tech., 21, 1575–1589, 2004. 3489, 3490, 3493, 3495, 3497, 3502

Souza, A.: How to understand Computational Fluid Dynamics Jargon, available at: http://www.nafems.org/downloads/edocs/how_to_understand_cfd_jargon-nafems.pdf, NAFEMS Ltd., 93 pp., 2005. 3492, 3493

Surry, D., Edey, R. T., and Murley, I. S.: Speed and direction correction factors for shipborne anemometers, Tech. rep., University of Western On-tario, London, ON, Canada, 1989. 3488

Thiebaux, M. L.: Wind tunnel experiments to determine cor-rection functions for shipborne anemometers, Tech. rep., Beford Institute of Oceanographyo, Dartmouth, NS, Canada, 1990. 3488

Webb, E. K., Pearman, G. I., and Leuning, R.: Correlation of flux measurement for density effects due to heat and water vapour transfer, Roy. Meteorol. Soc.., 106, 85–100, 1980. 3487

Yelland, M., Moat, B., Taylor, P., Pascal, R., Hutchings, J., and Cornell, V.: Wind stress measurements from the open ocean corrected for airflow distortion by the ship, J. Oceanogr., 28, 1511–1526, 1998. 3489

Yelland, M., Moat, B., Taylor, P., Pascal, R., and Berry, D.: CFD model estimates of the airflow distortion over research ships and the impact on momentum flux measurements, J. Atmos. Ocean. Tech., 19, 1477–1499, 2002. 3489, 3490, 3502

OSD
9, 3485–3520, 2012

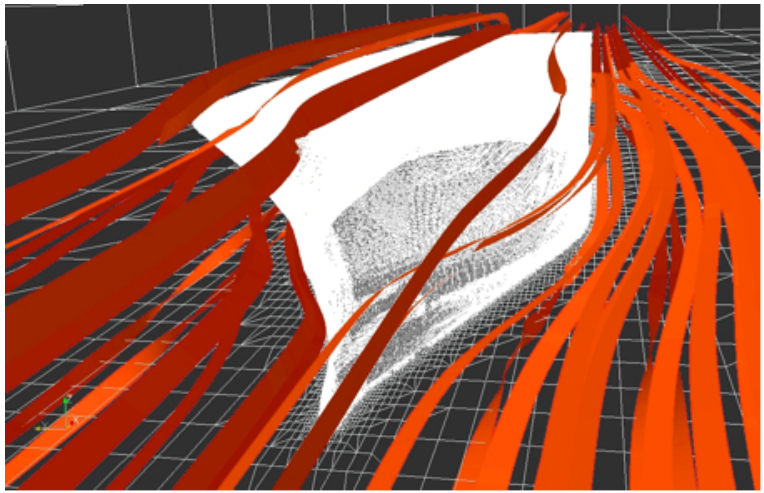

Fig. 1. Streamlines of distorted airflow by research vessels superstructure.

OSD
9, 3485–3520, 2012

Fig. 2. Photos of the two masts that have been used in this study: left is the single pole mast with a cross beam for the anemometers. Right shows the triangular lattice mast with the sonic located on a boom towards the bow.

OSD
9, 3485–3520, 2012

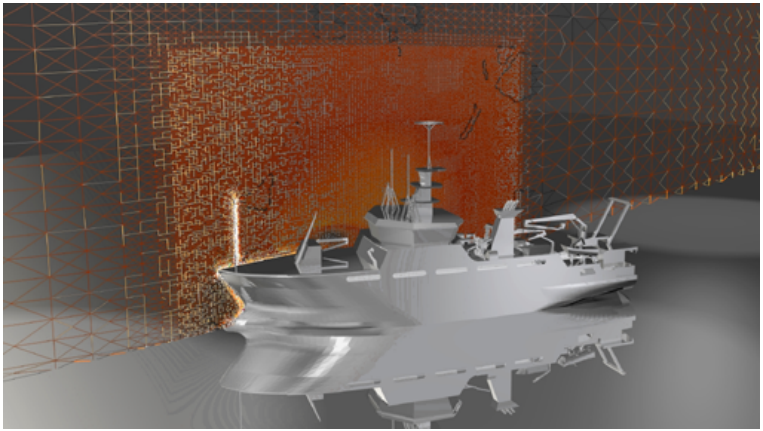

Fig. 3. R/V *Celtic Explorer* model with cross-section of hex mesh.

OSD
9, 3485–3520, 2012

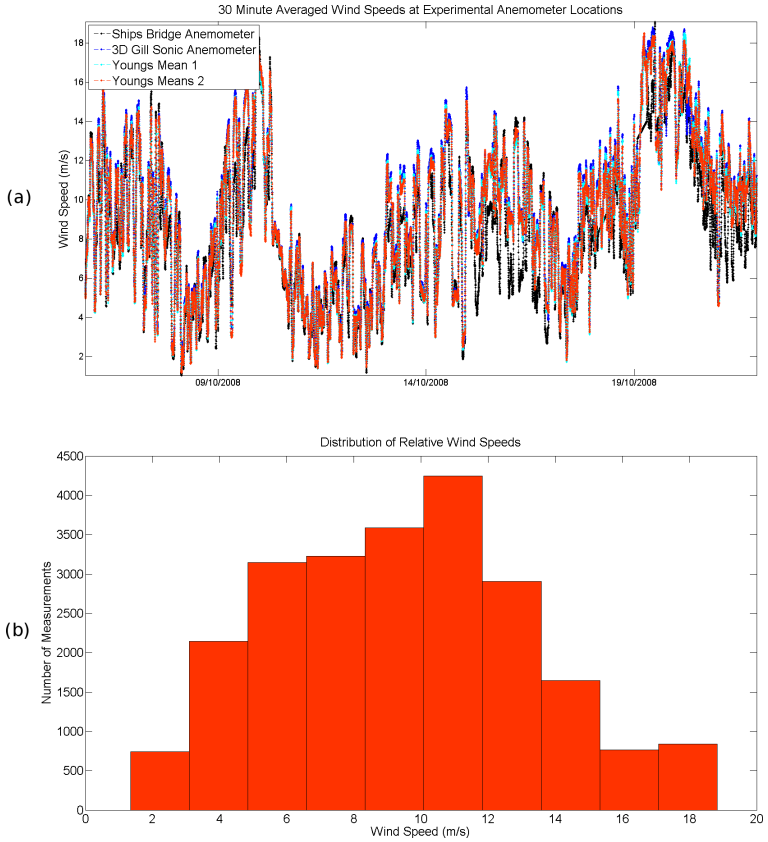

Fig. 4. (a) 30-min averaged true wind corrected measurements for bow Gill sonic anemometer, Young mean anemometer1 (Starboard), Young mean anemometer2 (Port) and bridge deck ultrasonic anemometer. **(b)** Histogram of distribution of measured wind speeds for chosen cruise period from bow sonic anemometer.

OSD
9, 3485–3520, 2012

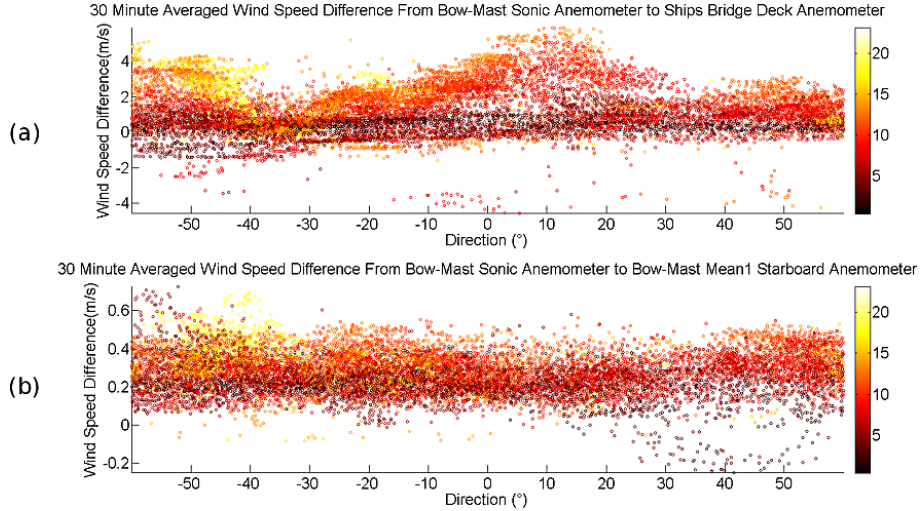

Fig. 5. 30-min averaged wind speed between **(a)** bow sonic anemometer and ship deck anemometer **(b)** bow sonic anemometer and Young starboard anemometer. The colour scale indicates wind direction differences.

OSD
9, 3485–3520, 2012

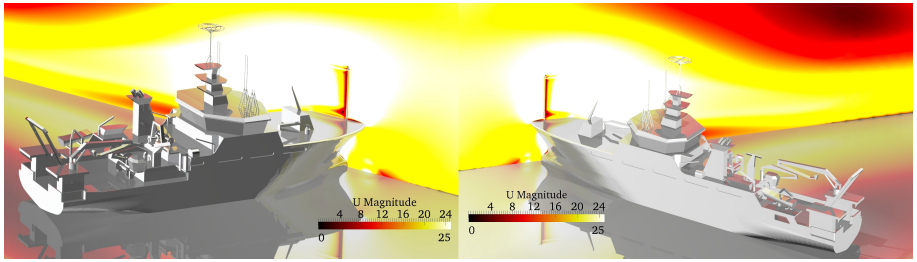

Fig. 6. (a) Flow speed over the ship for −60° and +60° to the bow for a steady state input stream of 25 m s^{-6}.

OSD
9, 3485–3520, 2012

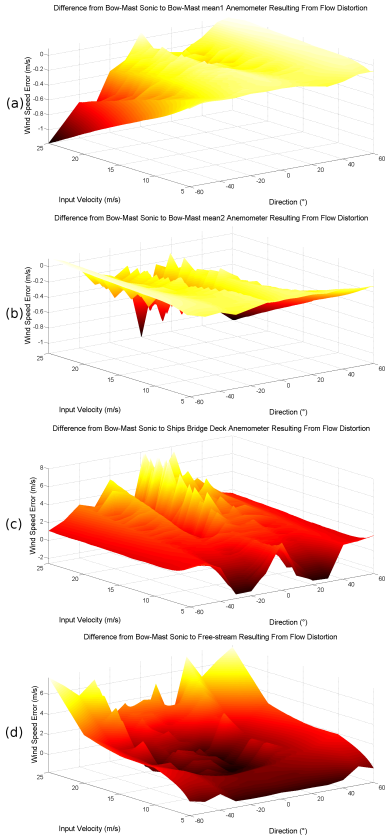

Fig. 7. Surface plot corrections for differences between **(a)** bow sonic and bow starboard **(b)** bow sonic and bridge sonic **(c)** bow sonic and port anemometer **(d)** bow sonic and free stream velocity.

OSD
9, 3485–3520, 2012

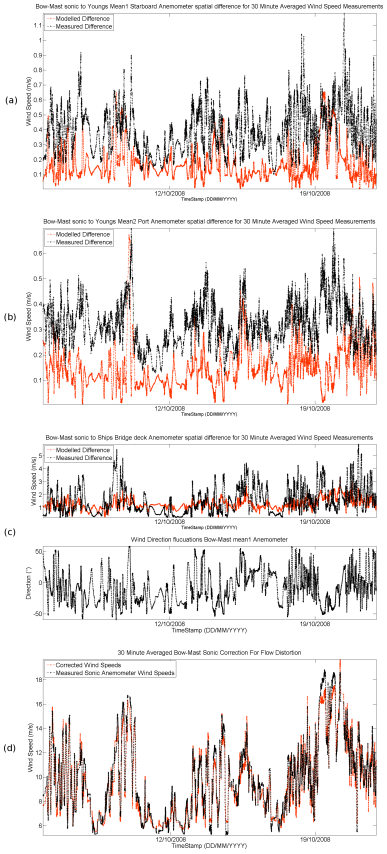

Fig. 8. Measured and modelled wind speeds differences for **(a)** bow sonic and bow starboard **(b)** bow sonic and bridge sonic **(c)** bow sonic and bow port anemometer (upper) and bow sonic direction (lower) **(d)** bow sonic and free stream velocity.

OSD
9, 3485–3520, 2012

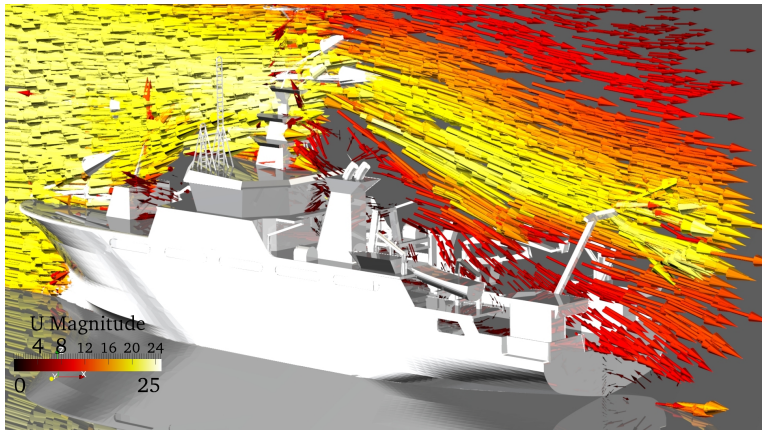

Fig. 9. Cross-sectional velocity vector plot from 5 to 25 m s^{-1}.

OSD
9, 3485–3520, 2012

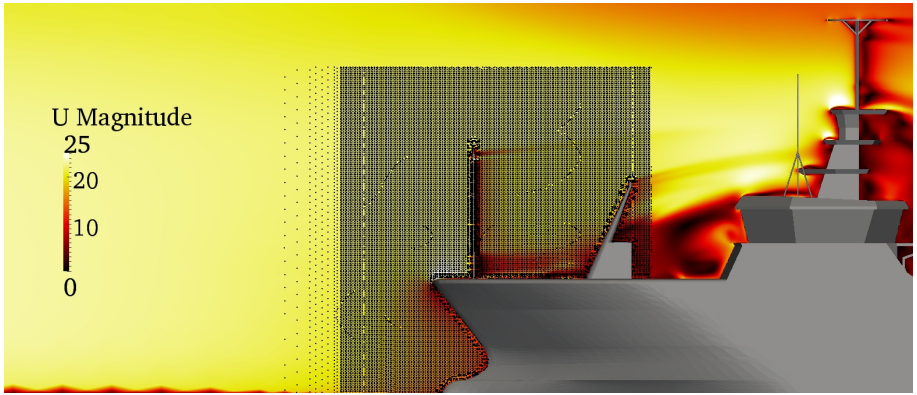

Fig. 10. Contour plot for optimised position of bow sonic anemometer.

OSD
9, 3485–3520, 2012

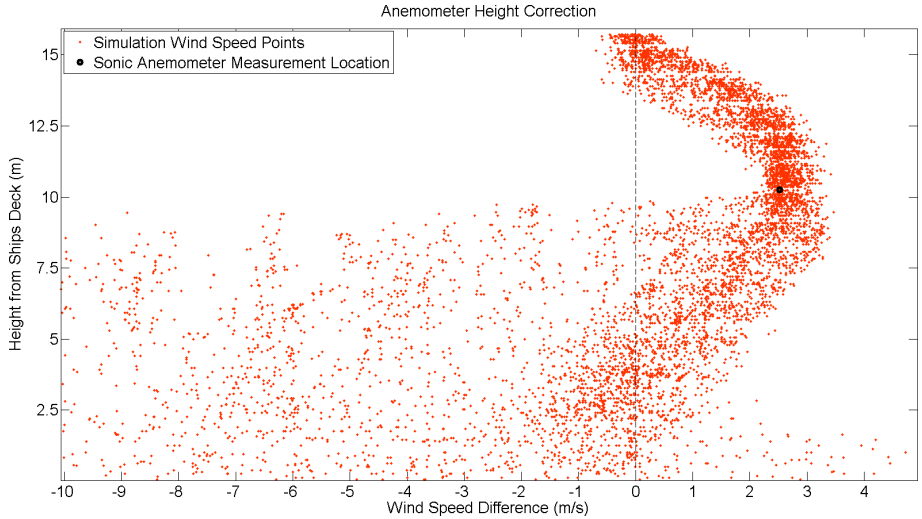

Fig. 11. Wind speed to free-stream difference with respect to change in height from bow deck. The black dot indicates the location of the sonic anemometer.

OSD
9, 3485–3520, 2012

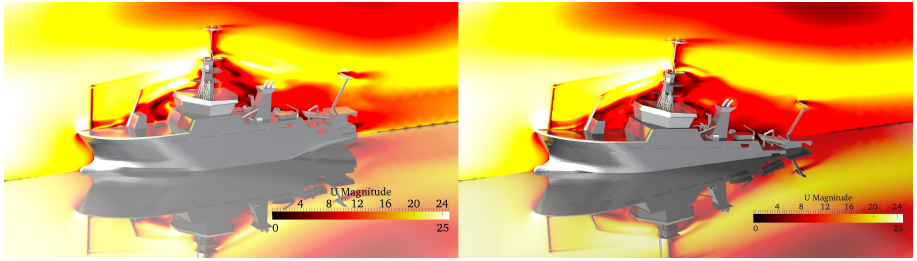

Fig. 12. Flow speed over the ship for 0° and +6° tilt for a steady state input stream of 25 m s^{-1}

OSD
9, 3485–3520, 2012

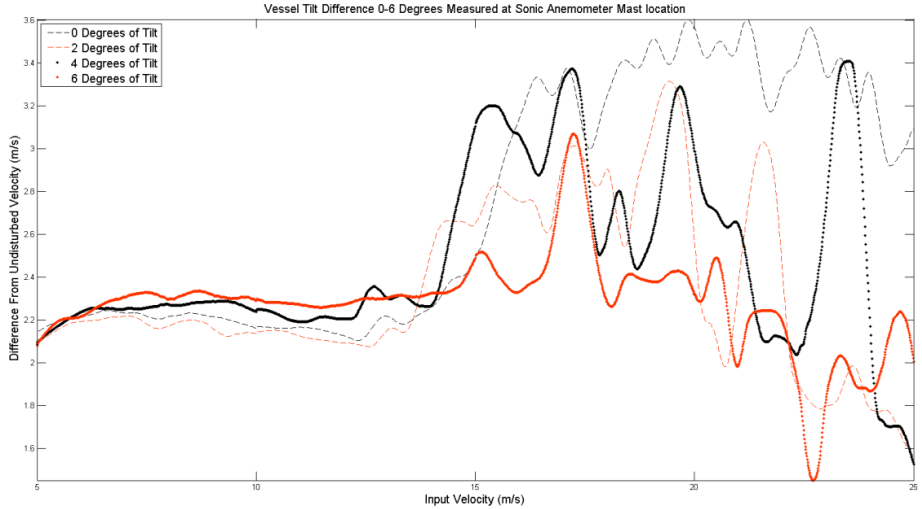

Fig. 13. Modelled difference from undisturbed flow over 0 to 25 m s^{-1} for tilt angle of 0, 2, 4, 6°.

OSD
9, 3485–3520, 2012

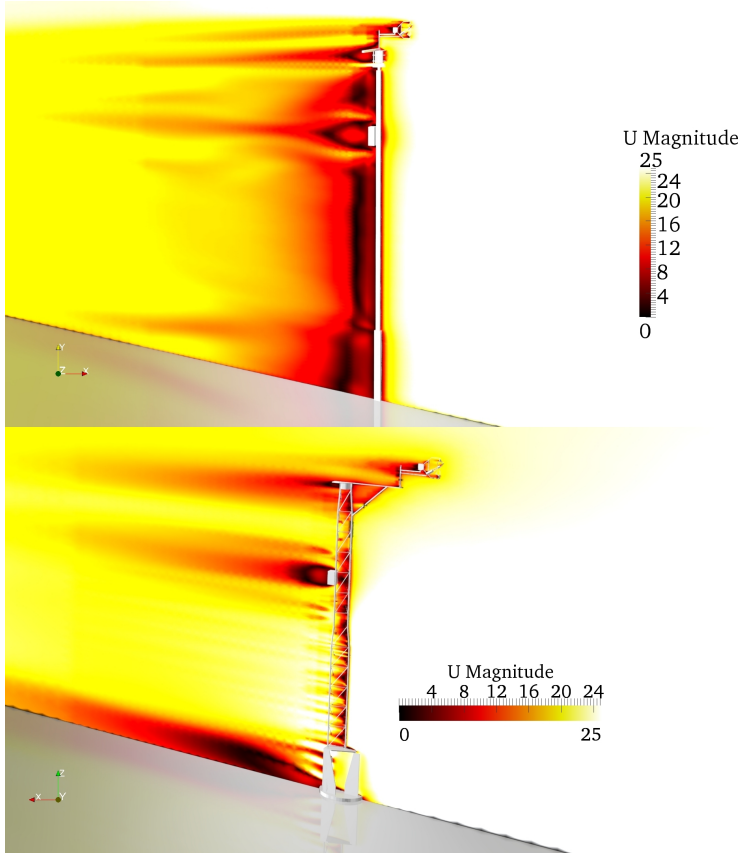

Fig. 14. Modelled velocities for each of the two masts for an input velocity of 25 m s^{-1}

OSD
9, 3485–3520, 2012

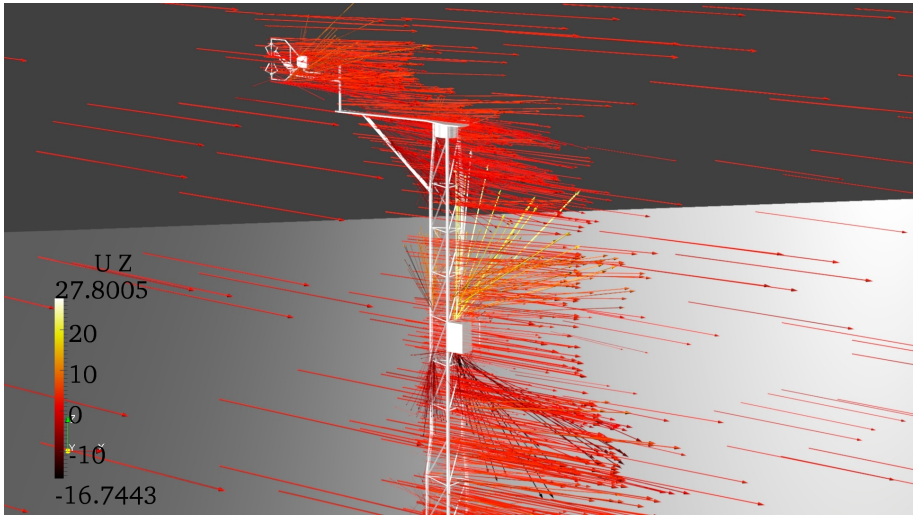

Fig. 15. Cross-sectional velocity vectors scaled from 5–25 m s^{-1} and 0°.

OSD
9, 3485–3520, 2012